Journal of Physics and Chemistry of Solids 181 (2023) 111532

Contents lists available at ScienceDirect

Journal of Physics and Chemistry of Solids

journal homepage: www.elsevier.com/locate/jpcs

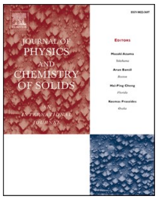

Enhancing the performance of the perovskite solar cells by modifying the SnO_2 electron transport layer

Biplav Dahal [a], Rui Guo [a], Rajesh Pathak [b], Melorina Dolafi Rezaee [a], Jeffrey W. Elam [b], Anil U. Mane [b], Wenzhi Li [a,*]

[a] Department of Physics, Florida International University, Miami, FL, 33199, USA
[b] Applied Materials Division, Argonne National Laboratory, Lemont, IL, 60439, USA

ARTICLE INFO

Keywords:
Perovskite solar cells
Tin oxide
Rubidium chloride
Electron transport layer modification
Defect passivation

ABSTRACT

The tin oxide (SnO_2) electron transport layer (ETL) plays a vital role in the photo-conversion efficiency (PCE) and stability of organic-inorganic perovskite solar cells (PSCs). However, SnO_2 ETL-induced defects such as hydroxyl groups, oxygen vacancies, exposed Sn atoms, and dangling bonds hinder device performance. In this study, rubidium chloride (RbCl) has been used to modify the SnO_2 ETL. Perovskite film formed on the RbCl-modified SnO_2 ETL exhibits improved crystallinity with enlarged grain size and reduced grain boundaries and enhanced optical absorption. The Hall-effect measurements indicate the improved carrier mobility, and the dark J-V curve shows the increment of electrical conductivity for the RbCl-modified SnO_2 ETL. X-ray photoelectron spectroscopy (XPS) results demonstrate the surface defects passivation of the perovskite layer by modifying the SnO_2 ETL. A champion PCE of 19.35% has been achieved for the RbCl-modified SnO_2 ETL-based devices with improved stability, while the control devices with unmodified SnO_2ETL show a PCE of 17.18%.

1. Introduction

In 2022, the best research cell efficiency for the organic-inorganic perovskite solar cells (PSCs) has reached 25.7%, which is not very far behind the power conversion efficiency (PCE) of commercially available silicon (Si) heterostructure-based solar cells (26.7%) [1]. The rapid evolution of PSCs is ascribed to long carrier diffusion length, low exciton binding energy, high carrier mobility, tunable bandgap, and high absorption coefficient of the perovskite materials [2,3]. PSCs incorporate an active perovskite layer between the electron transport layer (ETL) and hole transport layer (HTL). In the typical n-i-p structure, the crystal orientation, grain size, and quality of the perovskite layer directly depend on the surface chemistry of ETL because the perovskite layer is deposited on the n-type ETL. Hence the development and modification of ETL have become one of the major research subjects for the PSC research community.

For traditional planar n-i-p PSCs, titanium dioxide (TiO_2) was used as ETL [4–8]. Recently, tin oxide (SnO_2) has evolved as a promising ETL because of its unique advantages over TiO_2 including high electron mobility, deep conduction band, appropriate energy level, low crystallization temperature, and good chemical stability [9–14]. However, the oxygen vacancies in the SnO_2 film are the primary source of bulk and surface defects, which could capture charge carriers and reduce carrier mobility [15]. Additionally, unsaturated Sn dangling bonds can be formed at the SnO_2 surface. Those dangling bonds can absorb O_2 and H_2O in the ambient atmosphere, trap electrons, and form potential barriers obstructing electron transport [16]. Other significant issues with SnO_2 thin film as ETL include poor crystallinity and degraded conductivity of the low-temperature processed SnO_2 film [17]. Since the perovskite layer is deposited on top of ETL, the quality of the perovskite layer and the properties at the perovskite/ETL interface depend on the surface conditions of ETL. Therefore, numerous effective surface modification and interface engineering techniques have been practiced to minimize charge carrier recombination and improve interfacial energy level alignment, carrier generation, and carrier transfer. For instance, Zhang et al. employed the room-temperature synthesized $CsPbBr_3$ nanocrystals to modify the interface between perovskite and ETL. This modification enabled the seed-mediated growth of the perovskite, which further passivated the perovskite/ETL interface and reduced defects in the perovskite film [18]. Further, interface modification also plays a vital role in the morphology control of perovskite film by optimizing the film surface or interface and removing trap states [19,20].

---

* Corresponding author.
E-mail address: Wenzhi.Li@fiu.edu (W. Li).

https://doi.org/10.1016/j.jpcs.2023.111532
Received 9 March 2023; Received in revised form 18 June 2023; Accepted 27 June 2023

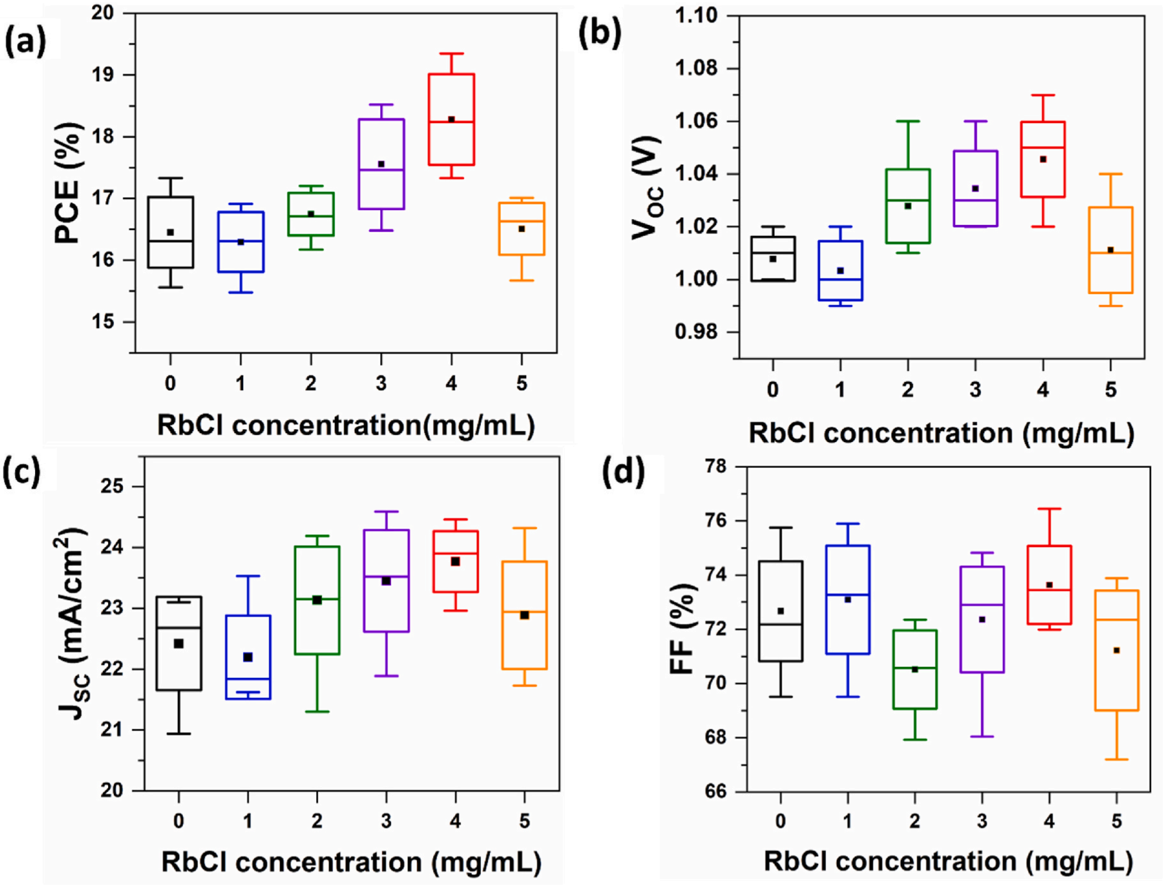

Fig. 1. Box diagrams of device parameters of PSCs with different RbCl concentrations: (a) PCE, (b) V_{OC}, (c) J_{SC}, and (d) FF. Each box plot includes 9 devices prepared under the same conditions.

With the sole purpose of enhancing the performance of PSCs, several methods have been explored to modify SnO_2 ETL, including elemental doping [21–23], compositing SnO_2 with other inorganic and organic materials, etc. [24–29]. Defects and grain boundaries within the perovskite layer and at the interface between perovskite and transport layers can trap charge carriers; hence, high-quality perovskite film with large and uniform grains is critical to achieve highly efficient PSCs [30]. Wang et al. used KCl as an interlayer between ETL and perovskite to observe the passivation effect and improve the crystallinity of the perovskite layer [31]. Cations and/or anions from ionic salts can effectively passivate surface defects such as hydroxyl groups, oxygen vacancies, exposed Sn atoms, and dangling bonds. Zhu et al. claimed that for the devices using SnO_2–KCl composite ETL, K^+ can occupy the interstitial lattice sites of perovskite to passivate the grain boundaries and enlarge the grain size, while Cl^- can hinder the formation of deep-trap defects at the SnO_2/perovskite interface [32]. Furthermore, the modification of ETL can enhance charge collection and transport, consequently improving the film conductivity and suppressing charge recombination. Gong et al. modified SnO_2 ETL with ammonium fluoride (NH_4F) and reported better carrier concentration, mobility, and electrical conductivity. They attributed these improvements to the diffusion of F^- ions into the SnO_2, which reduced the band offset between ETL and perovskite layer and increased the open-circuit voltage (V_{OC}) [33]. In another work, Jung et al. reported the bifunctional surface treatment of SnO_2 using NH_4F and claimed that the ammonium cation reacts with hydroxyl defect on SnO_2 to heal the defect by forming ammonia gas and water vapor [34]. Several other researchers modified SnO_2 ETL using cost-effective materials to enhance the performance of the perovskite solar cells [35,36].

Herein, we have successfully synthesized efficient and stable $MAPbI_3$ PSCs by modifying the SnO_2 ETL with RbCl. RbCl crystallites exhibit polyhedral structures and lattice parameters similar to those of perovskite crystallites, which are beneficial for the seed-mediated growth of the perovskite film [37]. While preparing this manuscript, Zhao et al. reported the improved stability of the perovskite phase by employing RbCl to convert excess lead iodide (PbI_2) into a passive inactive $(PbI_2)_2RbCl$ [38]. We have prepared the precursor solution for the modified SnO_2 ETL by mixing RbCl with the SnO_2 colloidal solution. On RbCl-modified SnO_2 ETLs, we obtained $MAPbI_3$ perovskite film with improved crystallinity, enlarged grain size, reduced grain boundaries, and enhanced optical absorption. Moreover, we have observed the surface defects passivation of the perovskite layer by modifying the ETL. The RbCl modification to the SnO_2 ETL significantly helped the effective electron transfer of the ETL towards the FTO, improved carrier mobility of the ETL, and increased the electrical conductivity of the ETL.

2. Experimental section

2.1. Materials

Lead iodide (PbI_2, 99.999% trace metal basis, perovskite grade), 4-*tert*-butylpyridine (4-TBP, 96%), lithium bis(trifluoromethanesulphonyl)imide (Li-TFSI, 99.95%), methylamine solution (MA, 33 wt% in absolute ethanol), 2,2′,7,7′-tetrakis[*N*,*N*-di(4-methoxyphenyl)amino]-9,9′-spirobifluorene (spiro-OMeTAD, 96%) were purchased from Sigma Aldrich. Methylammonium iodide (MAI, >99.5%, recrystallized 4 times) was bought from Lumtec. Anhydrous acetonitrile (ACN, 99.9%, Acroseal) and chlorobenzene (CB, 99.8%) were purchased from ACROS Organics. Tin (IV) oxide (SnO_2) colloidal precursor (15 wt% in H_2O colloidal dispersion) and rubidium chloride

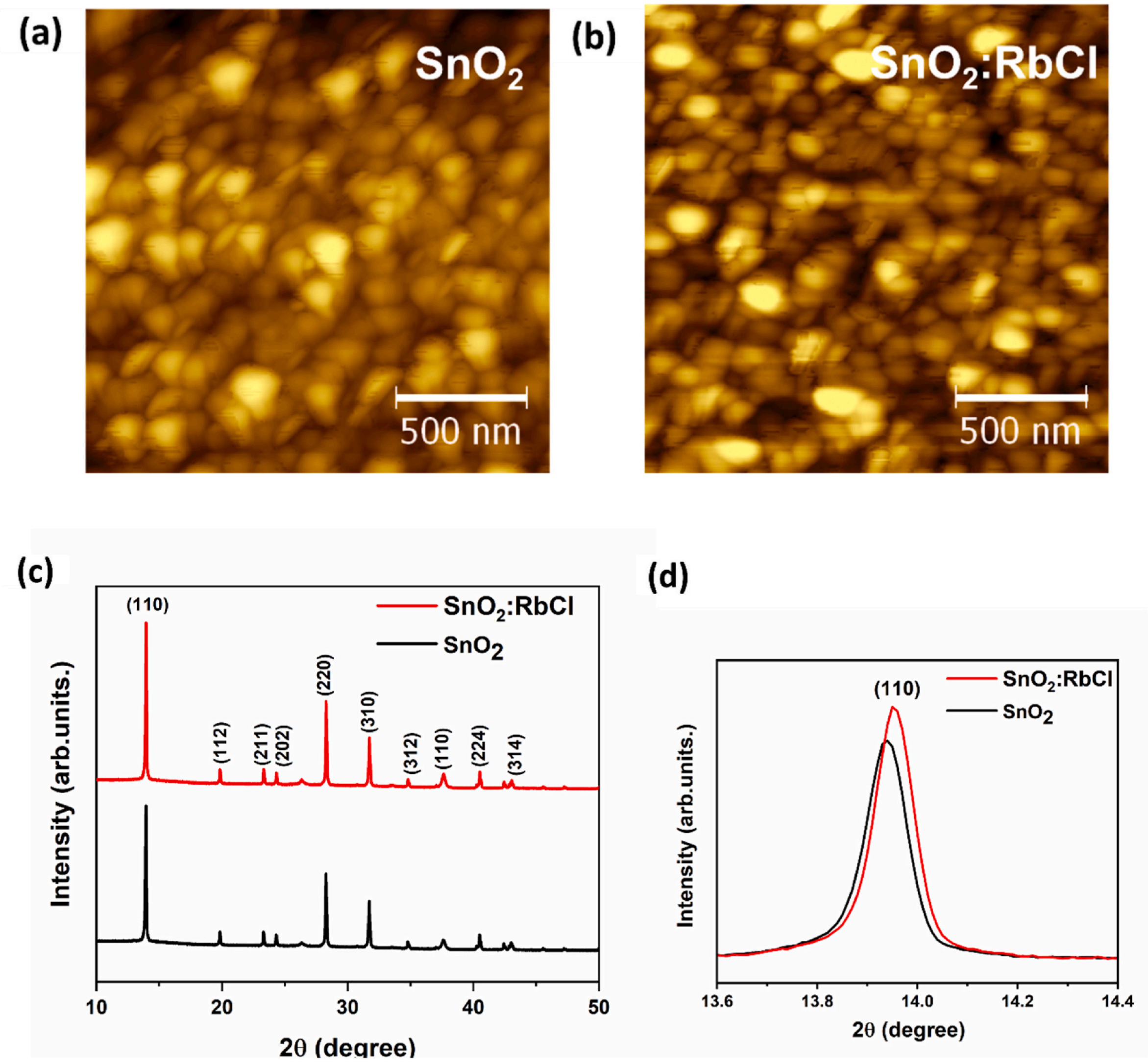

Fig. 2. (a, b) AFM images of the control SnO$_2$ and modified SnO$_2$ ETLs. (c) XRD patterns of the perovskite films deposited on control SnO$_2$ and modified SnO$_2$ ETLs. (d) XRD patterns for (110) peak of the perovskite films deposited on control and modified SnO$_2$ ETLs.

(RbCl, 99% metal basis) were purchased from Alfa Aesar. These chemical reagents mentioned above are commercially available and were directly used without processing.

2.2. Perovskite precursor preparation

The MAPbI$_3$ perovskite precursor solution was prepared in an ambient environment, and the one-step spin-coating technique was employed to deposit MAPbI$_3$ thin film. First, the precursor solution was prepared by mixing 190.8 mg MAI (1.2 mmol) and 553.2 mg PbI$_2$ (1.2 mmol) in 2 mL ACN. After stirring the mixture for 15 min, a black mixture of MAPbI$_3$ and unreacted PbI$_2$ and MAI was formed, which was dissolved by passing MA gas through the mixture solution to obtain a clear, transparent, and light-yellow precursor solution. The schematic illustration of the experimental setup to dissolve the black mixture in ACN using MA gas is shown in our previous work [11]. Then, a PTFE syringe filter with pore sizes of 0.2 μm was used to filter and remove any large particles.

2.3. PSC device fabrication

Pre-patterned glass/FTO substrates (Suzhou Solarflex Optoelectronic Technology Co., LTD) were cleaned sequentially in detergent water, deionized water, acetone, and ethanol for 15 min, respectively, under ultra-sonication. Before depositing ETL, the FTO glasses were dried and exposed to UV-ozone (Harrick Plasma, PDC-32G) for 15 min. The precursor solution for ETL was prepared for the control device by diluting the SnO$_2$ colloidal dispersion solution to 8 wt% by deionized water. For the modified device, SnO$_2$–RbCl mixed precursor solution was prepared by dissolving different concentrations of RbCl (1 mg/mL, 2 mg/mL, 3 mg/mL, 4 mg/mL, and 5 mg/mL) in the diluted SnO$_2$ solution. SnO$_2$-based ETL was deposited on the FTO substrate by spin-coating 55 μL of precursor solution at 4000 rpm for 30 s, then annealing the substrates at 180 °C for 90 min in the air. The substrates were then treated with UV-ozone for 10 min before depositing perovskite.

The MAPbI$_3$ perovskite precursor (55 μL) was spin-coated on the ETLs at 2000 rpm for 20 s, and the substrates were annealed in the presence of MA gas at 100 °C for 5 min. The precursor solution for HTL was prepared by dissolving 72.3 mg of spiro-OMeTAD, 28.8 μL of 4-TBP, and 17.5 μL of Li-TFSI solution (520 mg of Li-TFSI in 1 mL ACN) in 1 mL of CB. The spiro-OMeTAD solution (60 μL) was spin-coated on the perovskite film at 4000 rpm for 40 s. Finally, the gold (Au) electrode was deposited using an e-beam evaporator to the spiro-OMeTAD layer at a 10^{-6}torr vacuum pressure.

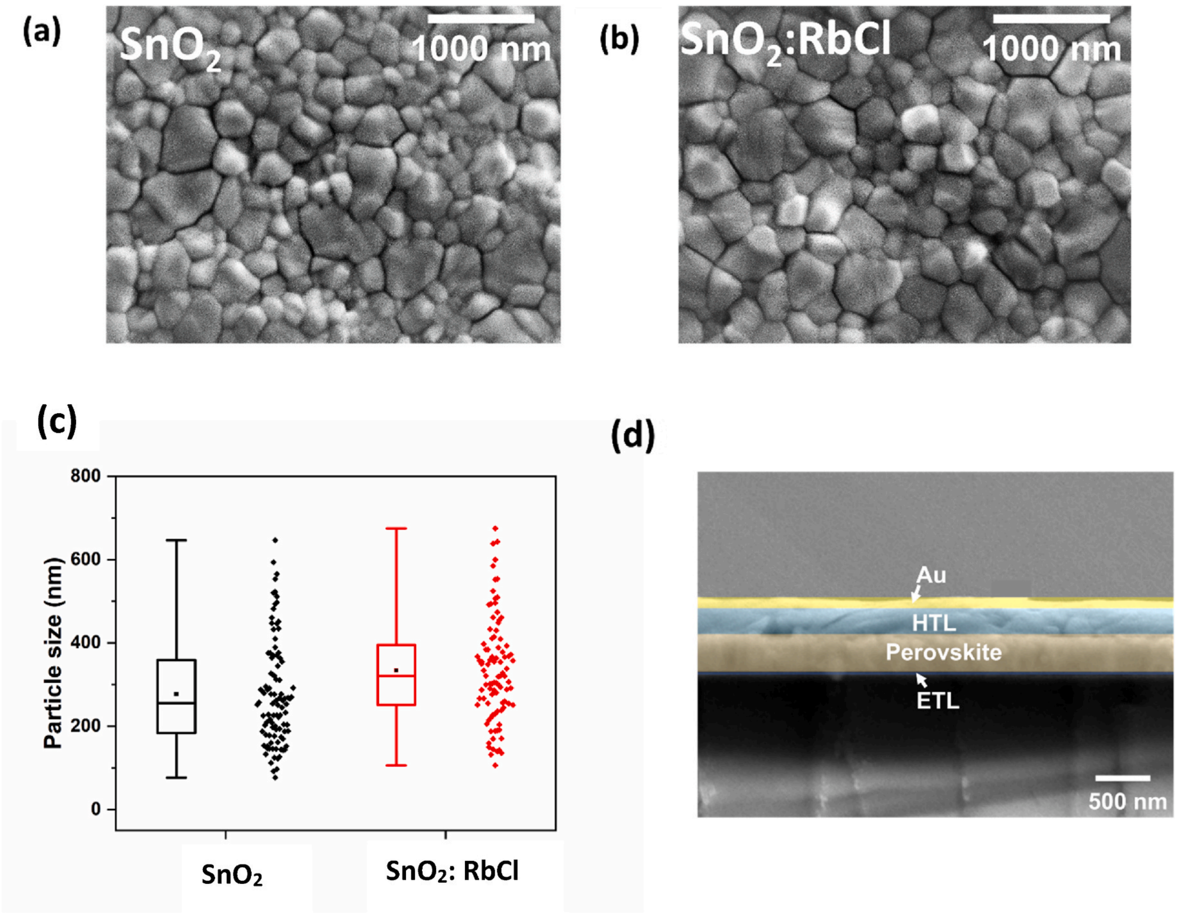

Fig. 3. (a, b) Top view SEM images of the perovskite films deposited on control SnO_2 and modified SnO_2 ETLs. (c) Box plot for comparing the perovskite grain size deposited on control and modified SnO_2 ETLs. (d) Cross-sectional SEM image of the PSC device (the different layers were colored to distinguish them).

2.4. Characterization

The morphology of the perovskite film was observed by a field emission scanning electron microscope (FE-SEM, JEOL 6330F). Atomic force microscopy (AFM) (Veeco Multimode Nanoscope III D) was used to determine the surface roughness of the ETL. The XRD profiles of the perovskite films were obtained by siemens diffraktometer D5000 with Cu Kα radiation ($\lambda = 1.54$ Å). The XPS measurements were carried out on a Thermo Fisher k-Alpha+, and the spectra were analyzed using Thermo Fisher Avantage software. All the spectra were referenced to the C1s peak at 284.8 eV. Optical absorption properties were carried out by UV–Vis spectrometer (Agilent Cary 5000 UV–Vis–NIR). The steady-state photoluminescence (PL) was measured on perovskite/ETL/FTO architecture using the excitation power of 290 μW, excited by a laser diode at a wavelength of 532 nm. Hall effect measurements (HMS-5300/AMP55T) were performed with van der Pauw geometry at room temperature. The J-V curve of the solar cell was measured using a source meter (Keithley 2400) under the AM 1.5G condition from a solar simulator (Newport).

3. Results and discussions

The typical device structure of the planar n-i-p perovskite solar cells is shown in Fig. S1 (see the supplementary information), where SnO_2 film is the ETL, $MAPbI_3$ is the perovskite layer, spiro-OMeTAD is the HTL, and Au is the electrode. This study aimed at modifying the SnO_2 ETL by incorporating RbCl and studying the performance of the modified device. The precursor solutions, Figs. S1(b) and (c), were used to spin-coat the control and modified ETL. The schematic of the spin-coating process of ETL is shown in Fig. S1(d).

The first step was to optimize the RbCl concentration in SnO_2 colloidal solution. We have fabricated 9 devices for each sample with different RbCl concentrations. Fig. 1 shows the box plot, which summarizes the photovoltaic parameters of PCE, open-circuit voltage (V_{OC}), short-circuit current density (J_{SC}), and fill factor (FF) of the devices synthesized with various concentrations (0, 1, 2, 3, 4, and 5 mg/ml) of RbCl in SnO_2 colloidal solutions. Each box in the plot represents the parameter distribution of 9 devices under the same working conditions. The box edges represent the 25–75 percentile. The whiskers outside the box represent the maximum and minimum observed data sets. The small square symbols (■) inside the boxes represent the mean, whereas the horizontal lines across the boxes represent the median. The PSCs prepared with 4 mg/mL RbCl concentration gave the best performance with the highest mean values of V_{OC}, J_{SC}, and FF (Fig. 1(b–d)) among all the devices, resulting in the best mean values of PCE as shown in Fig. 1(a). The average PCE for the control device is 16.45%, and for the modified (PSCs with SnO_2 ETL treated with 4 mg/mL RbCl) device is 18.28%. The excess of RbCl (5 mg/mL) shows a decrease in the performance of the device, which is likely due to charge trapping and de-trapping centers induced by the excessive Rb^+, as well as potential crystal distortion caused by its occupancy of substitution sites [39]. In addition, the low device performance can also be attributed to an increased average series resistance at higher RbCl concentrations (Fig. S2), resulting in reduced charge transport from the perovskite to the SnO_2 ETL [32]. Hence, 4 mg/mL is the optimum concentration of RbCl, and it will be used to modify SnO_2 ETL in the following texts.

The effect of ETL modification on the morphology and crystallinity of perovskite films is shown in Fig. 2. AFM was used to determine the

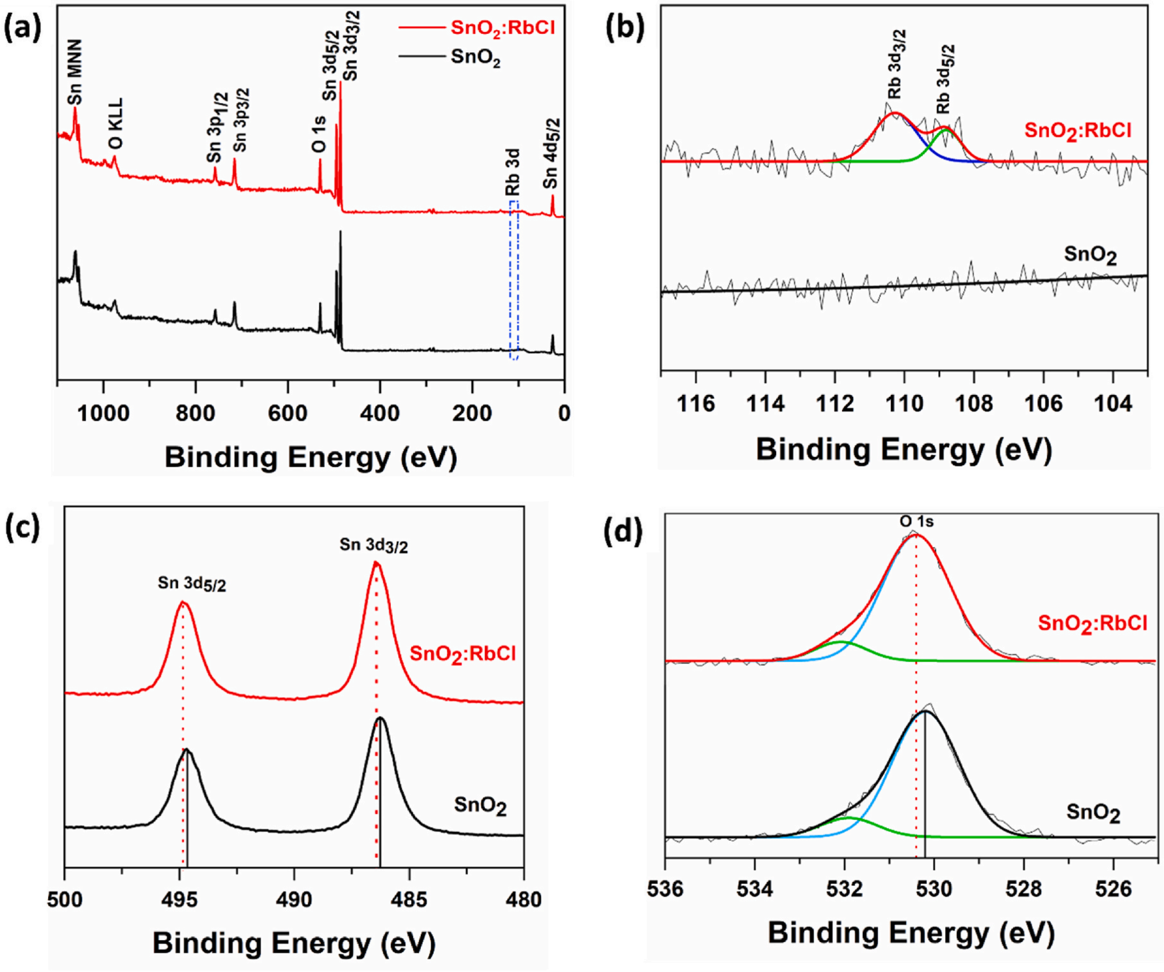

Fig. 4. (a) XPS survey scan of control SnO$_2$ and RbCl modified SnO$_2$ ETLs. High-resolution XPS spectra of (b) Rb 3d, (c) Sn 3d, and (d) O 1s.

Table 1
Parameters of deconvoluted O 1s peaks for SnO$_2$ and RbCl modified SnO$_2$ thin films.

O 1s peaks	SnO$_2$		RbCl modified SnO$_2$	
	FWHM (eV)	Area (%)	FWHM (eV)	Area (%)
O–Sn^{4+}	0.67418	86.80	0.67663	88.24
OH$^-$	0.61982	13.20	0.48959	11.76

surface roughness of the SnO$_2$ ETL with and without RbCl modification, as shown in Fig. 2(a) and (b). The root mean square (RMS) roughness is 7.73 nm for the pristine SnO$_2$ film, while it is 4.97 nm for the RbCl-modified SnO$_2$. The smaller roughness of the modified film suggests that the RbCl fills in the gaps between FTO valleys and makes the surface flatter [40], which is beneficial for the growth of perovskite. Fig. 2(c) shows the XRD patterns of perovskite layers formed on control and modified SnO$_2$ films. The XRD patterns on control film reveal the strongest diffraction peaks at 2θ angles of 14°, 28.3°, and 31.8°, which correspond to the tetragonal phase of MAPbI$_3$ [41]. The XRD spectra for the control and modified perovskite film clearly show that no PbI$_2$ phase is present, suggesting a complete perovskite conversion of the precursors. In addition, the XRD patterns suggest that the modification does not affect the crystallization behavior in terms of preferred growth direction. However, we observed the enhanced diffraction peak intensity of the (110) and (220) planes for the modified films. For the control film, the full width at half maximum (FWHM) of the (110) and (220) peaks are 0.098° and 0.117°, respectively, whereas, for the modified film, they are 0.093° and 0.112°. The decrease of FWHM indicates an effective improvement of the crystal quality with an enlarged grain size of MAPbI$_3$ films formed on RbCl-modified SnO$_2$ ETL. According to the Debye-Scherrer equation, FWHM and grain size have an inverse relationship [42]. Further, we observed a subtle deviation of XRD peaks to a higher angle in the modified film. Fig. 2(d) shows the deviation of the (110) peaks. This difference in the diffraction peak position may be attributed to the reduced strain in the perovskite crystal deposited on the modified SnO$_2$ ETL, resulting in improved crystal quality of the perovskite film [43].

SEM was employed to obtain the morphology images of the perovskite film, and ImageJ software was used to measure the grain size. The top-view SEM images, Fig. 3(a) and (b), illustrate the smooth and dense perovskite films on both control and modified SnO$_2$ films. The average grain size reached 333 nm for the modified perovskite, whereas 277 nm for the control film, Fig. 3(c). The larger grain size of the perovskite film would enhance the device's performance by reducing the grain boundaries. Grain boundaries generally contain deep-level bulk defects such as ion vacancies and interstitial defects. Reducing the grain boundaries helps reduce the bulk defects and the overall nonradiative losses in PSC by lowering the number of trapping sites and scattering sources of the charge carriers [44,45]. The crystallite size of the perovskite films was also calculated using the Debye–Scherrer equation and the XRD data. It was found that the crystallite size increased from 141.4 nm for the controlled films to 149.1 nm for those fabricated with 4 mg/mL RbCl, which is in good agreement with the results from the SEM images. The crystallite size appears smaller than the grain size because an individual

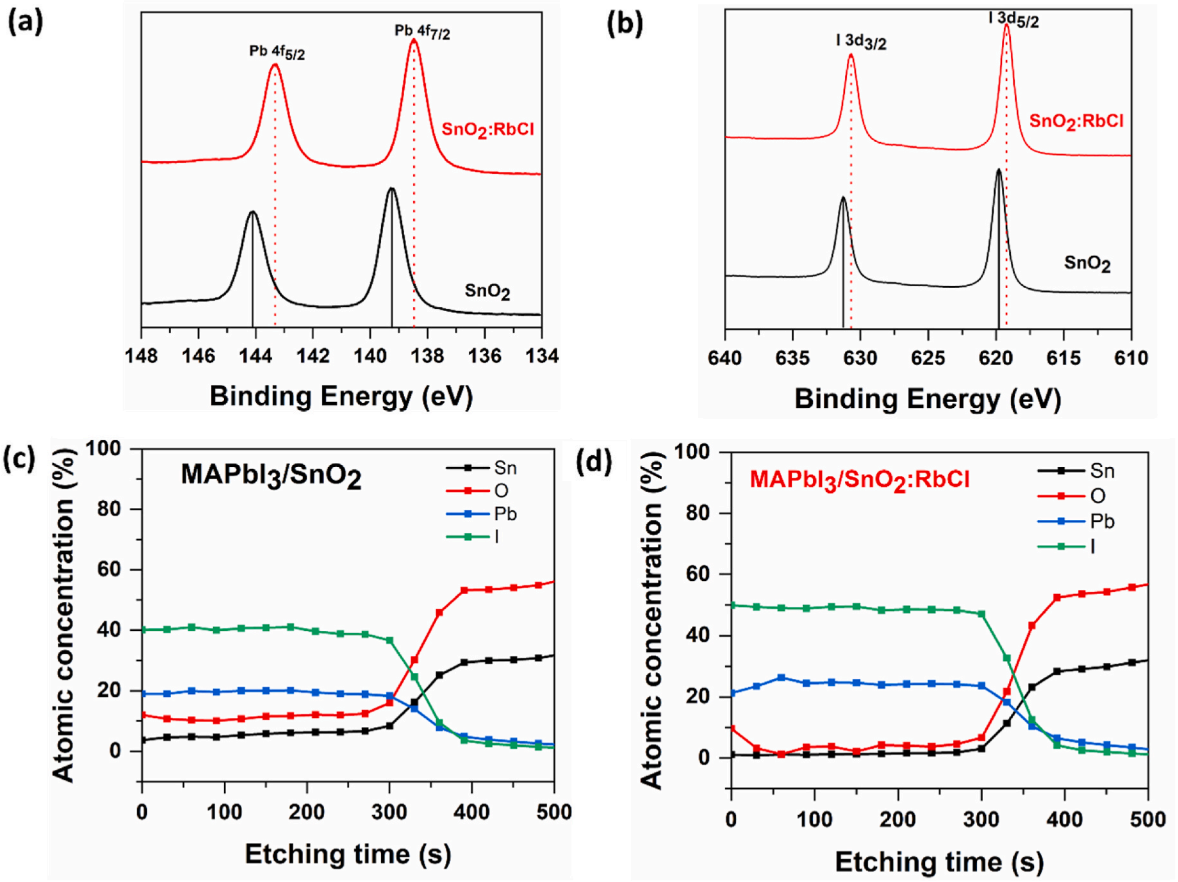

Fig. 5. XPS spectra of (a) Pb 4f and (b) I 3d of perovskite layers deposited on control SnO_2 and RbCl-modified SnO_2 ETLs. Compositional depth profiles generated by XPS for the (c) control and (d) modified samples with the structure $MAPbI_3/SnO_2/FTO$.

grain may consist of multiple crystallites. The cross-sectional SEM image of the PSC device shown in Fig. 3(d) reveals that the thickness of the electron transport layer is 35 nm, the perovskite layer is 400 nm, the hole transport layer is 225 nm, and the gold layer is 90 nm. Further, we analyzed the composition and element ratio of $MAPbI_3$ film using Energy Dispersive Spectroscopy (EDS) and determined the relative element ratio of Iodine (I) and lead (Pb) as 2.25 and 2.53 for control and modified perovskite films, respectively, which shows a close agreement with the stoichiometry of 3 for the modified perovskite film. We also observed a slightly lower atomic percentage of Oxygen (O) in the modified film. The atomic percentage of different elements is shown in Table S1 (for the control film) and Table S2 (for the modified film). Furthermore, EDS-mapping (Fig. S3) reveals that the distribution of Pb and I is similar across both control and modified films, indicating the uniformity of the perovskite film.

XPS was employed to study the chemical state of control and modified SnO_2 ETL. The XPS survey spectra are shown in Fig. 4(a). For the control ETL, the XPS spectrum is dominated by Sn and O peaks as expected for the SnO_2 surface [46] and shows a small adventitious carbon peak at 284.8 eV. The XPS spectrum for the RbCl-modified SnO_2 ETL sample is similar to the SnO_2 control sample but exhibits peaks at 110.18 eV and 108.76 eV, which correspond to the Rb $3d_{3/2}$ and $3d_{5/2}$ states, respectively, as shown in the high-resolution XPS scan, Fig. 4(b) [47]. High-resolution scans of the Sn 3d region are shown in Fig. 4(c). The Sn $3d_{3/2}$ and Sn $3d_{5/2}$ peaks appear in the SnO_2 control sample at 486.26 eV and 494.66 eV, respectively, but shift to higher energies by ~0.20 eV after RbCl modification demonstrating the alteration in the chemical environment of Sn. The higher binding energy may indicate an increase in electron density around the Sn atom due to Cl^- bound to SnO_2. Fig. 4(d) shows a high-resolution XPS scan of the O 1s region. In this figure, the O 1s peak is deconvoluted into two components at 530.19 eV and 531.91 eV that we assign to the O^{2-} state in SnO_2 and chemisorbed oxygen atoms or hydroxyl groups on the SnO_2 surface, respectively [48]. The slight shift in the O 1s peak to higher binding energy for the modified ETL suggests the increased stoichiometry of SnO_2 by forming O–Sn^{4+} bond. Table 1 depicts the parameters of deconvoluted O 1s peaks as O–Sn^{4+} and OH^- for SnO_2 and RbCl-modified SnO_2 thin films. The FWHM values of the peak of O–Sn^{4+} are almost the same for both control (0.67418 eV) and modified SnO_2 (0.67663 eV), whereas the FWHM values of the peak of OH^- decreased from 0.61982 eV for the control SnO_2 to 0.48959 eV for the RbCl modified SnO_2. OH^- acts as trap states and reduces the effectiveness of electron transport. The decrease in FWHM value and area of OH^- peak suggest the reduction in the oxygen vacancies, attributed to the facilitation of electron transport by reducing the trap states [35]. Further, RbCl can bond to the surface of SnO_2 and passivate the oxygen vacancy (or uncoordinated Sn) by forming a Lewis adduct of Cl^- and uncoordinated Sn on the surface of the SnO_2 [49].

XPS measurements were further used to investigate the binding energy changes of I^- and uncoordinated Pb^{2+} in $MAPbI_3$ film upon modification of SnO_2 ETL. Fig. 5(a) shows that the Pb $4f_{7/2}$ and Pb $4f_{5/2}$ signals at 139.25 eV and 144.10 eV detected for the $MAPbI_3$ perovskite film deposited on SnO_2 ETL are shifted to lower binding energies by 0.79 eV for the $MAPbI_3$ perovskite film deposited on RbCl-modified SnO_2 ETL. The decrease in binding energy suggests the decrease of the cationic charge of Pb^{2+} ions within $MAPbI_3$, which may be due to the donation of electron pairs on the Cl atom to the empty 6p orbital of Pb^{2+} [50]. As depicted in Fig. 5(b), the I 3d peaks of the $MAPbI_3$ film deposited on RbCl-modified SnO_2 ETL shifted to the lower binding energies compared to those of the $MAPbI_3$ film formed on unmodified SnO_2

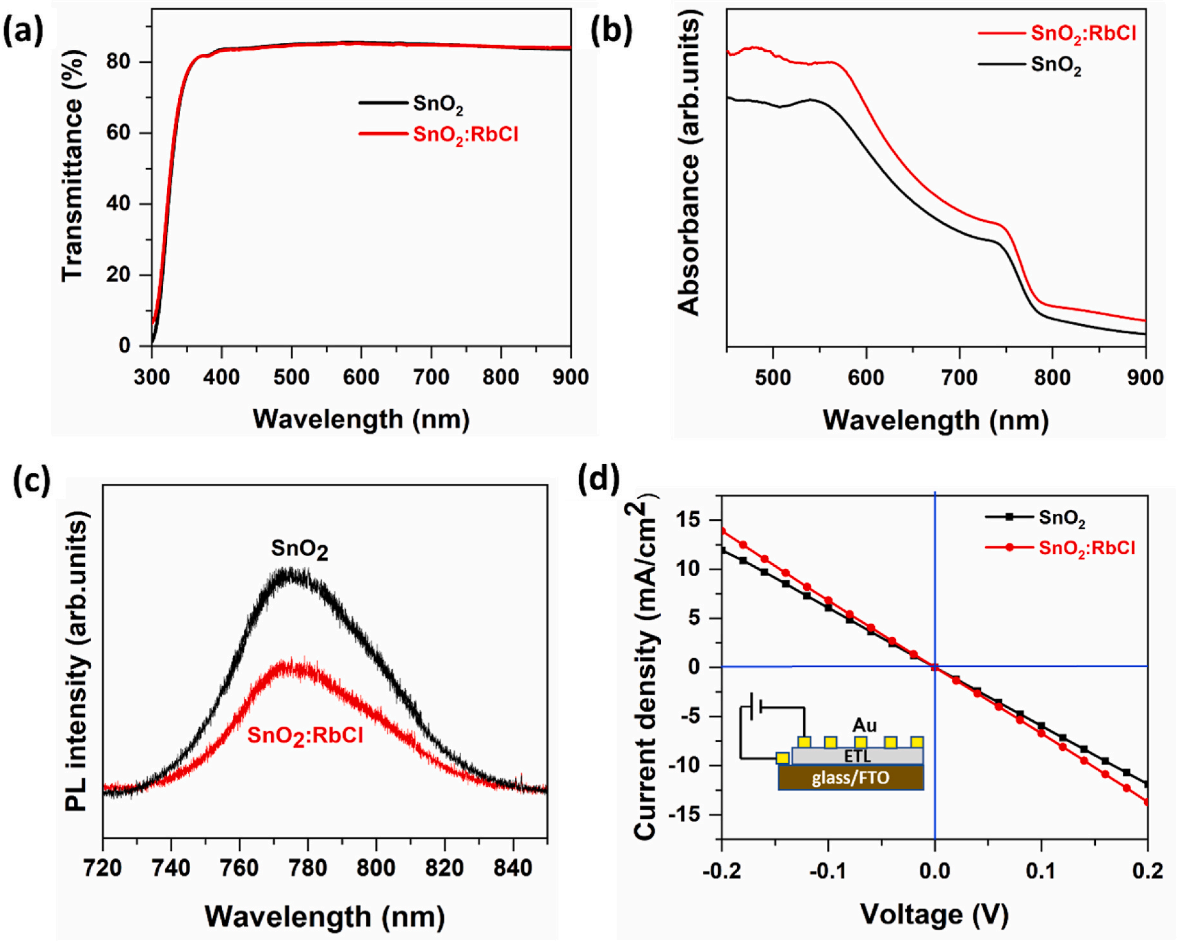

Fig. 6. (a) Transmittance of control SnO_2 and RbCl-modified SnO_2 ETLs. (b) Absorption spectra of perovskite films deposited on control and RbCl-modified ETLs. (c) PL spectra of perovskite films deposited on control and RbCl-modified ETLs. (d) Dark J–V curves of SnO_2films without or with RbCl modification in FTO/ETL/Au structure.

Table 2
Electrical parameters obtained from the Hall effect measurements for SnO_2 and RbCl-modified SnO_2 ETLs.

RbCl concentration (mg/mL)	Mobility (cm^2/Vs)	Sheet concentration of carriers (/cm^2)	Bulk concentration of carriers (/cm^3)	Hall Coefficient (cm^3/C)
0	19.51	-2.90×10^{16}	-7.26×10^{20}	-8.59×10^{-3}
4	24.82	-2.10×10^{16}	-5.26×10^{20}	-1.19×10^{-2}

ETL, suggesting interactions between iodine and rubidium ions, which may passivate I^- defects by suppressing the free migration of I^- [51]. XPS depth profiles on $MAPbI_3/SnO_2$/FTO for the control and modified sample are shown in Fig. 5(c) and (d), respectively. At the top surface layer, before etching has started, the relative ratios of I to Pb are 2.11 and 2.74 for control and modified samples, respectively. For the stoichiometry of $MAPbI_3$, the relative ratio of I to Pb should be 3. The relative ratio of I to Pb for the control film is less than that for the modified film, which is consistent with the findings from the EDS analysis. This is due to the higher relative degradation of the control perovskite film, suggesting that the modified sample possesses better surface stability than the control sample. Moreover, the perovskite layer deposited on the unmodified SnO_2 shows the presence of oxygen throughout the perovskite layer, whereas the perovskite layer deposited on the RbCl-modified SnO_2, the oxygen concentration reduces to almost zero after a few seconds of etching. This result is attributed to the passivation of surface defects in the perovskite layer by modifying the SnO_2 ETL with RbCl, which prevents oxygen from penetrating deep into the perovskite layer [52].

The optical transmission spectra of control and RbCl-modified SnO_2 ETLs are shown in Fig. 6(a). Both ETLs exhibit transmittance above 80% in the visible wavelength ranging from 380 to 750 nm. Fig. 6(b) shows that the absorbance of the perovskite films in the visible wavelength range increases after the RbCl surface modification. The enhanced absorbance for the perovskite film with RbCl-modified ETL is due to the increased grain size and improved crystallinity of the perovskite film, consistent with our results from XRD and SEM images. Fig. 6(c) shows steady-state PL responses for the perovskite layer deposited on control and RbCl-modified SnO_2 ETLs. When a PL measurement is taken, an excitation source is used to cause electrons within the perovskite layer to be excited to a higher energy conduction band and holes to form in a lower energy valence band. These electron-hole pairs interact and recombine, releasing energy as photons which is detected and measured by a PL instrument. The lower PL intensity for a perovskite layer deposited on a RbCl-modified ETL compared to one deposited on a control SnO_2 ETL suggests that the RbCl modification reduces the rate of exciton recombination. We further performed Hall effect measurements (Table 2) of control and modified ETL. The negative Hall coefficients and carrier concentrations (sheet and bulk) represent the n-type conductivity of the SnO_2 ETL. There is a slight decrement in sheet concentration and bulk concentration of charge carriers for the modified SnO_2 ETL

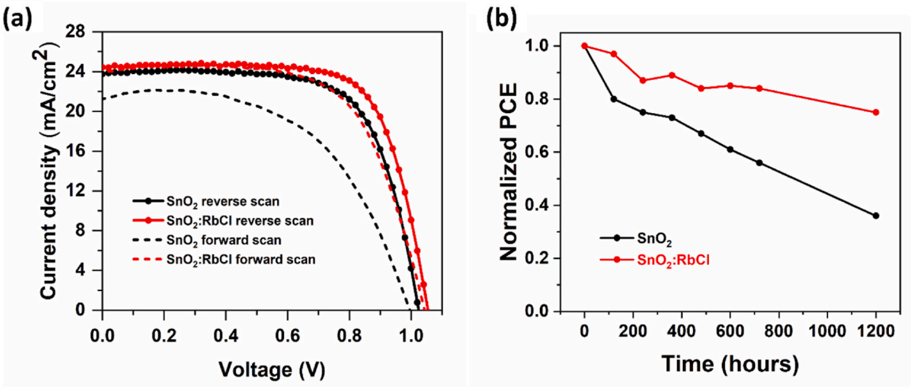

Fig. 7. (a) J-V curves of PSCs based on SnO_2 and RbCl-modified SnO_2 ETLs. (b) Time variation of PCE of unencapsulated devices exposed to conditions with 25 ± 5% RH at room temperature.

Table 3
Photovoltaic parameters of the champion PSCs based on SnO_2 and RbCl-modified SnO_2 ETLs.

RbCl concentration (mg/ml)	Scan direction	V_{OC} (V)	J_{SC} (mA/cm^2)	FF (%)	PCE (%)	HI
0	Reverse	1.02	23.49	71.48	17.18	0.179
	Forward	1	21.29	66.11	14.10	
4	Reverse	1.05	24.26	76.44	19.35	0.123
	Forward	1.04	23.96	68.78	16.96	

film, indicating the intrinsic defect concentration (oxygen vacancy O_i and tin interstitial Sn_i) became lower for the RbCl-modified SnO_2 film. For the control SnO_2 film, those intrinsic defects produce shallow donor levels and lead to large carrier concentration and low carrier mobility [53]. The Hall mobility of RbCl-modified SnO_2 ETL is 24.82 $cm^2\ V^{-1}\ s^{-1}$, which is higher than that of control SnO_2 ETL (19.51 $cm^2\ V^{-1}\ s^{-1}$). The increment of carrier mobility of the RbCl-modified SnO_2 ETL is attributed to the enhanced crystallinity [54]. In addition, Rb^+ ions may provide additional valence electrons to the SnO_2 lattice and increase the electron extraction and transfer ability of the SnO_2 ETL. Furthermore, as shown in Fig. 6(d), the dark J-V curve illustrates that the RbCl-modified SnO_2 film exhibits a higher conductivity than the control film. The electrical conductivity of the SnO_2 film shows an enhancement of ~14% after the RbCl modification, implying the n-type doping effect of the Cl^- ions.

The J-V curves of PSCs based on SnO_2 and RbCl-modified SnO_2 ETLs under both reverse and forward scan are shown in Fig. 7(a). The photovoltaic parameters of the champion devices are listed in Table 3. Under reverse scan direction, the PCE of the PSC based on RbCl-modified SnO_2 ETL is 19.35%, whereas the PCE of the PSC based on the pristine SnO_2 ETL is 17.18%. The increased PCE of the PSC based on RbCl-modified SnO_2 ETL is attributed to the improvement in J_{SC}, V_{OC}, and FF. The increased conductivity and improved electron mobility of the RbCl-modified SnO_2 ETL led to the enhancement of the J_{SC} of the PSC. Similarly, the improved FF of the PSC based on RbCl-modified SnO_2 ETL demonstrates better carrier transport due to favorable changes in the morphology of the perovskite film and improved conductivity of the ETL. The V_{OC} increment for the PSCs with RbCl-modified SnO_2 ETL may be ascribed to the defects passivation and reduced recombination. Moreover, the hysteresis of the modified devices slightly reduced with the hysteresis index (HI) decreasing from 0.179 to 0.123. The smaller hysteresis is attributed to the good contact between ETL and perovskite with enhanced charge transport ability at the ETL/perovskite interface. Finally, we have compared the ambient stability of the PSCs based on SnO_2 and RbCl-modified SnO_2 ETLs. As shown in Fig. 7(b), the PSC based on a RbCl-modified SnO_2 ETL shows better stability, retaining 75.12% of its initial PCE after 50 days of exposure to the ambient conditions (25 ± 5% relative humidity, room temperature). On the other hand, the PSC based on unmodified SnO_2 ETL maintains 36.10% of its initial PCE under the same condition. The enhanced stability for the PSC based on RbCl-modified SnO_2 ETL is attributed to the reduced grain boundaries and defect passivation.

4. Conclusion

In summary, the RbCl modification to the SnO_2 ETL demonstrated an effective approach to enhancing the performance of $MAPbI_3$ planar perovskite solar cells. The perovskite film deposited on RbCl-modified SnO_2 ETL showed enlarged grain size, high crystallinity, and enhanced visible range absorbance. In addition, the RbCl modification to SnO_2 ETL passivates the I^- defects of perovskite by suppressing the free migration of I^-. Moreover, after the modification, Rb^+ ions may provide additional valence electrons to the SnO_2 lattice and increase the electron extraction and transfer ability of SnO_2 ETL towards the FTO. Furthermore, the RbCl-modified SnO_2 film exhibits a higher conductivity than the unmodified SnO_2 film. Consequently, the champion PSC based on RbCl-modified SnO_2 ETL yields a PCE of 19.35% with improved stability. This work demonstrates that RbCl is a promising modifier of SnO_2 ETL for the n-i-p planar $MAPbI_3$ PSCs with enhanced performance.

Declaration of competing interest

The authors declare that they have no known competing financial interests or personal relationships that could have appeared to influence the work reported in this paper.

Data availability

Data will be made available on request.

Acknowledgments

This work is supported by the National Science Foundation under grants 1506640 and 2213923. The authors would like to acknowledge the support from Advanced Materials Engineering Research Institutes (AMERI) at Florida International University. The authors are grateful to Dr. Hebin Li for the help with PL measurements, Dr. Deidra Hodges for the help with Hall measurements, and Dr. Christopher Dares for providing access to his laboratory for UV–Vis measurements.

Appendix A. Supplementary data

Supplementary data to this article can be found online at https://doi.org/10.1016/j.jpcs.2023.111532.

References

[1] NREL, Best Research-Cell Efficiencies. https://www.nrel.gov/pv/cell-efficiency.html, 2022. (Accessed 1 May 2022).

[2] S.D. Stranks, G.E. Eperon, G. Grancini, C. Menelaou, M.J.P. Alcocer, T. Leijtens, L. M. Herz, A. Petrozza, H.J. Snaith, Electron-hole diffusion lengths exceeding 1 micrometer in an organometal trihalide perovskite absorber, Science 342 (2013) (1979) 341, https://doi.org/10.1126/science.1243982.

[3] M.A. Green, A. Ho-Baillie, H.J. Snaith, The emergence of perovskite solar cells, Nat. Photonics 8 (2014) 506–514, https://doi.org/10.1038/nphoton.2014.134.

[4] A. Yella, L.-P. Heiniger, P. Gao, M.K. Nazeeruddin, M. Grätzel, Nanocrystalline rutile electron extraction layer enables low-temperature solution processed perovskite photovoltaics with 13.7% efficiency, Nano Lett. 14 (2014) 2591–2596, https://doi.org/10.1021/nl500399m.

[5] R. Wu, B. Yang, J. Xiong, C. Cao, Y. Huang, F. Wu, J. Sun, C. Zhou, H. Huang, J. Yang, Dependence of device performance on the thickness of compact TiO2 layer in perovskite/TiO2 planar heterojunction solar cells, J. Renew. Sustain. Energy 7 (2015), 043105, https://doi.org/10.1063/1.4926578.

[6] C. Chen, Y. Cheng, Q. Dai, H. Song, Radio frequency magnetron sputtering deposition of TiO2 thin films and their perovskite solar cell applications, Sci. Rep. 5 (2015), 17684, https://doi.org/10.1038/srep17684.

[7] Z. Yang, B. Cai, B. Zhou, T. Yao, W. Yu, S. (Frank) Liu, W.-H. Zhang, C. Li, An up-scalable approach to CH3NH3PbI3 compact films for high-performance perovskite solar cells, Nano Energy 15 (2015) 670–678, https://doi.org/10.1016/j.nanoen.2015.05.027.

[8] W. Zhou, J. Zhen, Q. Liu, Z. Fang, D. Li, P. Zhou, T. Chen, S. Yang, Successive surface engineering of TiO2 compact layers via dual modification of fullerene derivatives affording hysteresis-suppressed high-performance perovskite solar cells, J. Mater. Chem. A Mater. 5 (2017) 1724–1733, https://doi.org/10.1039/C6TA07876A.

[9] W. Ke, G. Fang, Q. Liu, L. Xiong, P. Qin, H. Tao, J. Wang, H. Lei, B. Li, J. Wan, G. Yang, Y. Yan, Low-temperature solution-processed tin oxide as an alternative electron transporting layer for efficient perovskite solar cells, J. Am. Chem. Soc. 137 (2015) 6730–6733, https://doi.org/10.1021/jacs.5b01994.

[10] H. Tang, Q. Cao, Z. He, S. Wang, J. Han, T. Li, B. Gao, J. Yang, D. Deng, X. Li, SnO2–Carbon nanotubes hybrid electron transport layer for efficient and hysteresis-free planar perovskite solar cells, Solar RRL 4 (2020), 1900415, https://doi.org/10.1002/solr.201900415.

[11] R. Guo, B. Dahal, A. Thapa, Y.R. Poudel, Y. Liu, W. Li, Ambient processed (110) preferred MAPbI3 thin films for highly efficient perovskite solar cells, Nanoscale Adv. 3 (2021) 2056–2064, https://doi.org/10.1039/D0NA01029D.

[12] Z. Qin, Y. Chen, X. Wang, X. Liu, Y. Miao, Y. Zhao, Incorporation of two-dimensional WSe2 into MAPbI3 perovskite for efficient and stable photovoltaics, J. Phys. Chem. Lett. 12 (2021) 6883–6888, https://doi.org/10.1021/acs.jpclett.1c02012.

[13] X. Zhuang, R. Sun, D. Zhou, S. Liu, Y. Wu, Z. Shi, Y. Zhang, B. Liu, C. Chen, D. Liu, H. Song, Synergistic effects of multifunctional lanthanides doped CsPbBrCl2 quantum dots for efficient and stable MAPbI3 perovskite solar cells, Adv. Funct. Mater. 32 (2022), 2110346, https://doi.org/10.1002/adfm.202110346.

[14] B. Dahal, W. Li, Configuration of methylammonium lead iodide perovskite solar cell and its effect on the device's performance: a review, Adv. Mater. Interfac. (2022), 2200042, https://doi.org/10.1002/admi.202200042 n/a.

[15] J. Xie, K. Huang, X. Yu, Z. Yang, K. Xiao, Y. Qiang, X. Zhu, L. Xu, P. Wang, C. Cui, D. Yang, Enhanced electronic properties of SnO2 via electron transfer from graphene quantum dots for efficient perovskite solar cells, ACS Nano 11 (2017) 9176–9182, https://doi.org/10.1021/acsnano.7b04070.

[16] S.Y. Park, K. Zhu, Advances in SnO2 for efficient and stable n–i–p perovskite solar cells, advanced materials, n/a, https://doi.org/10.1002/adma.202110438, 2022.

[17] D. Liu, Y. Wang, H. Xu, H. Zheng, T. Zhang, P. Zhang, F. Wang, J. Wu, Z. Wang, Z. Chen, S. Li, SnO2-Based perovskite solar cells: configuration design and performance improvement, Solar RRL 3 (2019), 1800292, https://doi.org/10.1002/solr.201800292.

[18] J. Zhang, L. Wang, C. Jiang, B. Cheng, T. Chen, J. Yu, CsPbBr3 nanocrystal induced bilateral interface modification for efficient planar perovskite solar cells, Adv. Sci. 8 (2021), 2102648, https://doi.org/10.1002/advs.202102648.

[19] B. Chaudhary, A. Kulkarni, A.K. Jena, M. Ikegami, Y. Udagawa, H. Kunugita, K. Ema, T. Miyasaka, Poly(4-Vinylpyridine)-Based interfacial passivation to enhance voltage and moisture stability of lead halide perovskite solar cells, ChemSusChem 10 (2017) 2473–2479, https://doi.org/10.1002/cssc.201700271.

[20] B. Yuan, C. Li, W. Yi, F. Juan, H. Yu, F. Xu, C. Li, B. Cao, PMMA passivated CsPbI2Br perovskite film for highly efficient and stable solar cells, J. Phys. Chem. Solid. 153 (2021), 110000, https://doi.org/10.1016/j.jpcs.2021.110000.

[21] G. Yang, H. Lei, H. Tao, X. Zheng, J. Ma, Q. Liu, W. Ke, Z. Chen, L. Xiong, P. Qin, Z. Chen, M. Qin, X. Lu, Y. Yan, G. Fang, Reducing hysteresis and enhancing performance of perovskite solar cells using low-temperature processed Y-doped SnO2 nanosheets as electron selective layers, Small 13 (2017), 1601769, https://doi.org/10.1002/smll.201601769.

[22] J. Bahadur, A.H. Ghahremani, B. Martin, T. Druffel, M.K. Sunkara, K. Pal, Solution processed Mo doped SnO2 as an effective ETL in the fabrication of low temperature planer perovskite solar cell under ambient conditions, Org. Electron. 67 (2019) 159–167, https://doi.org/10.1016/j.orgel.2019.01.027.

[23] Z. Xu, S.H. Teo, L. Gao, Z. Guo, Y. Kamata, S. Hayase, T. Ma, La-doped SnO2 as ETL for efficient planar-structure hybrid perovskite solar cells, Org. Electron. 73 (2019) 62–68, https://doi.org/10.1016/j.orgel.2019.03.053.

[24] M. Hu, L. Zhang, S. She, J. Wu, X. Zhou, X. Li, D. Wang, J. Miao, G. Mi, H. Chen, Y. Tian, B. Xu, C. Cheng, Electron transporting bilayer of SnO2 and TiO2 nanocolloid enables highly efficient planar perovskite solar cells, Solar RRL 4 (2020), 1900331, https://doi.org/10.1002/solr.201900331.

[25] J. Dagar, S. Castro-Hermosa, G. Lucarelli, F. Cacialli, T.M. Brown, Highly efficient perovskite solar cells for light harvesting under indoor illumination via solution processed SnO2/MgO composite electron transport layers, Nano Energy 49 (2018) 290–299, https://doi.org/10.1016/j.nanoen.2018.04.027.

[26] J. Wei, F. Guo, X. Wang, K. Xu, M. Lei, Y. Liang, Y. Zhao, D. Xu, SnO2-in-Polymer matrix for high-efficiency perovskite solar cells with improved reproducibility and stability, Adv. Mater. 30 (2018), 1805153, https://doi.org/10.1002/adma.201805153.

[27] J. Wang, K. Datta, C.H.L. Weijtens, M.M. Wienk, R.A.J. Janssen, Insights into fullerene passivation of SnO2 electron transport layers in perovskite solar cells, Adv. Funct. Mater. 29 (2019), 1905883, https://doi.org/10.1002/adfm.201905883.

[28] K. Liu, S. Chen, J. Wu, H. Zhang, M. Qin, X. Lu, Y. Tu, Q. Meng, X. Zhan, Fullerene derivative anchored SnO2 for high-performance perovskite solar cells, Energy Environ. Sci. 11 (2018) 3463–3471, https://doi.org/10.1039/C8EE02172D.

[29] G. Yang, C. Wang, H. Lei, X. Zheng, P. Qin, L. Xiong, X. Zhao, Y. Yan, G. Fang, Interface engineering in planar perovskite solar cells: energy level alignment, perovskite morphology control and high performance achievement, J. Mater. Chem. A Mater. 5 (2017) 1658–1666, https://doi.org/10.1039/C6TA08783C.

[30] H. do Kim, H. Ohkita, H. Benten, S. Ito, Photovoltaic performance of perovskite solar cells with different grain sizes, Adv. Mater. 28 (2016) 917–922, https://doi.org/10.1002/adma.201504144.

[31] P. Wang, J. Wang, X. Zhang, H. Wang, X. Cui, S. Yuan, H. Lu, L. Tu, Y. Zhan, L. Zheng, Boosting the performance of perovskite solar cells through a novel active passivation method, J. Mater. Chem. A Mater. 6 (2018) 15853–15858, https://doi.org/10.1039/C8TA05593A.

[32] P. Zhu, S. Gu, X. Luo, Y. Gao, S. Li, J. Zhu, H. Tan, Simultaneous contact and grain-boundary passivation in planar perovskite solar cells using SnO2-KCl composite electron transport layer, Adv. Energy Mater. 10 (2020), 1903083, https://doi.org/10.1002/aenm.201903083.

[33] X. Gong, Q. Sun, S. Liu, P. Liao, Y. Shen, C. Grätzel, S.M. Zakeeruddin, M. Grätzel, M. Wang, Highly efficient perovskite solar cells with gradient bilayer electron transport materials, Nano Lett. 18 (2018) 3969–3977, https://doi.org/10.1021/acs.nanolett.8b01440.

[34] E.H. Jung, B. Chen, K. Bertens, M. Vafaie, S. Teale, A. Proppe, Y. Hou, T. Zhu, C. Zheng, E.H. Sargent, Bifunctional surface engineering on SnO2 reduces energy loss in perovskite solar cells, ACS Energy Lett. 5 (2020) 2796–2801, https://doi.org/10.1021/acsenergylett.0c01566.

[35] J. Kim, J. Park, Y.-H. Kim, W. Jo, Improvement of open-circuit voltage deficit via pre-treated NH4+ ion modification of interface between SnO2 and perovskite solar cells, Small 18 (2022), 2204173, https://doi.org/10.1002/smll.202204173.

[36] J. Zhuang, P. Mao, Y. Luan, N. Chen, X. Cao, G. Niu, F. Jia, F. Wang, S. Cao, J. Wang, Rubidium fluoride modified SnO2 for planar n-i-p perovskite solar cells, Adv. Funct. Mater. 31 (2021), 2010385, https://doi.org/10.1002/adfm.202010385.

[37] X. Liu, B. Li, N. Zhang, Z. Yu, K. Sun, B. Tang, D. Shi, H. Yao, J. Ouyang, H. Gong, Multifunctional RbCl dopants for efficient inverted planar perovskite solar cell with ultra-high fill factor, negligible hysteresis and improved stability, Nano Energy 53 (2018) 567–578, https://doi.org/10.1016/j.nanoen.2018.09.023.

[38] Y. Zhao, F. Ma, Z. Qu, S. Yu, T. Shen, H.-X. Deng, X. Chu, X. Peng, Y. Yuan, X. Zhang, J. You, Inactive (PbI2)2RbCl stabilizes perovskite films for efficient solar cells, Science 377 (2022) (1979) 531–534, https://doi.org/10.1126/science.abp8873.

[39] L. Dong, L. Qiu, D. Mei, X. Ma, L. Song, J. Wang, J. Xiong, P. Du, NaCl-passivated and Na+-doped tin oxide electron transport layers enable highly efficient planar perovskite solar cells, J. Phys. Chem. Solid. 158 (2021), 110250, https://doi.org/10.1016/j.jpcs.2021.110250.

[40] Y. Tang, R. Roy, Z. Zhang, Y. Hu, F. Yang, C. Qin, L. Jiang, H. Liu, Rubidium chloride doping TiO2 for efficient and hysteresis-free perovskite solar cells with decreasing traps, Sol. Energy 231 (2022) 440–446, https://doi.org/10.1016/j.solener.2021.11.074.

[41] T. Baikie, Y. Fang, J.M. Kadro, M. Schreyer, F. Wei, S.G. Mhaisalkar, M. Graetzel, T. J. White, Synthesis and crystal chemistry of the hybrid perovskite (CH3NH3)PbI3 for solid-state sensitised solar cell applications, J. Mater. Chem. A Mater. 1 (2013) 5628–5641, https://doi.org/10.1039/C3TA10518K.

[42] B. Dahal, L. Joshi, S. Pandey, S. Shrestha, Effect of thiourea concentration on structural, optical and electrical properties of Cu2ZnSnS4 thin films prepared by using spray pyrolysis, Asian J.Chem.Sci. 2 (2017) 1–8, https://doi.org/10.9734/AJOCS/2017/34313.

[43] L. Hu, K. Sun, M. Wang, W. Chen, B. Yang, J. Fu, Z. Xiong, X. Li, X. Tang, Z. Zang, S. Zhang, L. Sun, M. Li, Inverted planar perovskite solar cells with a high fill factor and negligible hysteresis by the dual effect of NaCl-doped PEDOT:PSS, ACS Appl. Mater. Interfaces 9 (2017) 43902–43909, https://doi.org/10.1021/acsami.7b14592.

[44] D. Gedamu, I.M. Asuo, D. Benetti, M. Basti, I. Ka, S.G. Cloutier, F. Rosei, R. Nechache, Solvent-antisolvent ambient processed large grain size perovskite thin films for high-performance solar cells, Sci. Rep. 8 (2018), 12885, https://doi.org/10.1038/s41598-018-31184-0.

[45] Q. Cai, Z. Lin, W. Zhang, G. Shen, X. Wen, H. Dong, X. Xu, D. Zhu, C. Mu, Improvement performance of planar perovskite solar cells by bulk and surface defect passivation, ACS Sustain. Chem. Eng. 9 (2021) 13001–13009, https://doi.org/10.1021/acssuschemeng.1c04615.

[46] A.H. Ghahremani, B. Martin, A. Gupta, J. Bahadur, K. Ankireddy, T. Druffel, Rapid fabrication of perovskite solar cells through intense pulse light annealing of SnO2

and triple cation perovskite thin films, Mater. Des. 185 (2020), 108237, https://doi.org/10.1016/j.matdes.2019.108237.

[47] J. Chastain, R.C. King Jr., Handbook of X-ray photoelectron spectroscopy, Perkin-Elmer Corporation. 40 (1992) 221.

[48] X. Ren, D. Yang, Z. Yang, J. Feng, X. Zhu, J. Niu, Y. Liu, W. Zhao, S.F. Liu, Solution-processed Nb:SnO2 electron transport layer for efficient planar perovskite solar cells, ACS Appl. Mater. Interfaces 9 (2017) 2421–2429, https://doi.org/10.1021/acsami.6b13362.

[49] J. Yan, Z. Lin, Q. Cai, X. Wen, C. Mu, Choline chloride-modified SnO2 achieving high output voltage in MAPbI3 perovskite solar cells, ACS Appl. Energy Mater. 3 (2020) 3504–3511, https://doi.org/10.1021/acsaem.0c00038.

[50] B. Li, J. Zhen, Y. Wan, X. Lei, Q. Liu, Y. Liu, L. Jia, X. Wu, H. Zeng, W. Zhang, G.-W. Wang, M. Chen, S. Yang, Anchoring fullerene onto perovskite film via grafting pyridine toward enhanced electron transport in high-efficiency solar cells, ACS Appl. Mater. Interfaces 10 (2018) 32471–32482, https://doi.org/10.1021/acsami.8b11459.

[51] J. Zhang, H. Yu, Multifunctional dopamine-assisted preparation of efficient and stable perovskite solar cells, J. Energy Chem. 54 (2021) 291–300, https://doi.org/10.1016/j.jechem.2020.05.061.

[52] Y. Wu, D. Wang, J. Liu, H. Cai, Review of interface passivation of perovskite layer, Nanomaterials 11 (2021), https://doi.org/10.3390/nano11030775.

[53] J. Ma, X. Zheng, H. Lei, W. Ke, C. Chen, Z. Chen, G. Yang, G. Fang, Highly efficient and stable planar perovskite solar cells with large-scale manufacture of E-beam evaporated SnO2 toward commercialization, Solar RRL 1 (2017), 1700118, https://doi.org/10.1002/solr.201700118.

[54] X. Ling, J. Yuan, D. Liu, Y. Wang, Y. Zhang, S. Chen, H. Wu, F. Jin, F. Wu, G. Shi, X. Tang, J. Zheng, S. (Frank) Liu, Z. Liu, W. Ma, Room-temperature processed Nb2O5 as the electron-transporting layer for efficient planar perovskite solar cells, ACS Appl. Mater. Interfaces 9 (2017) 23181–23188, https://doi.org/10.1021/acsami.7b05113.